International Conference on Space Optics—ICSO 2020

Virtual Conference

30 March–2 April 2021

Edited by Bruno Cugny, Zoran Sodnik, and Nikos Karafolas

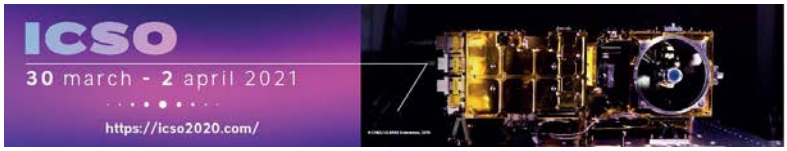

Instrumental development of NanoCarb, a new spectro-imaging sensor

International Conference on Space Optics — ICSO 2020, edited by Bruno Cugny, Zoran Sodnik, Nikos Karafolas, Proc. of SPIE Vol. 11852, 118523Z · © 2021 ESA and CNES
CCC code: 0277-786X/21/$21 · doi: 10.1117/12.2599632

Instrumental development of NanoCarb, a new spectro-imaging sensor

Florence de la Barrière*[1a], Yann Ferrec[a], Laurence Croizé[a], Hélène Ehrhardt[b], Silvère Gousset[b], Etienne Le Coarer[b]
[a]ONERA/DOTA, Chemin de la Hunière, BP 80100, 91123 Palaiseau Cedex, France; [b]Institut de Planétologie et d'Astrophysique de Grenoble, Université Grenoble-Alpes, 38058 Grenoble, France

ABSTRACT

Estimating emissions of the main greenhouse gases (such as CO_2 and CH_4) is a challenge in studying climate change. The European project called SCARBO, which involves several partners, aims at evaluating the feasibility of a low-cost constellation of small satellites onboarding small instruments, which could be capable of quantifying greenhouse gases. In this context, we propose NanoCarb, a miniature snapshot Fourier-transform imaging spectrometer concept dedicated to the measurement of two greenhouse gases: CO_2 and CH_4. Its compact design makes it a good candidate for small satellites. It is based on a multi-channel architecture which provides a sparse interferometric sampling strategy. This multi-channel design only involves two specific optical components: a microlens array and an interferometric plate, which is a stepcase phase plate. We have developed and assembled two NanoCarb prototypes which have been experimentally validated through a dedicated airborne campaign. This paper focuses on the design and laboratory calibrations of the two prototypes. The tests include both imaging and spectral features of the instruments. An adequate laboratory calibration is essential to process the data acquired by the prototypes during the airborne campaign. Experimental results show the good quality of the prototypes.

Keywords: Air pollution monitoring, anthropogenic greenhouse gas emissions, Fourier transform spectrometry, optical instrumentation, passive remote sensing

1. INTRODUCTION

Anthropic activity impact on climate change is a scientific and politic key challenge [1]. It is supported by the universal climate agreement (Paris, 2015). The methodology used to estimate greenhouse gas emissions is generally based on "bottom-up" methodology, i.e. based on activity statistics and emission factors specific to each source. However, these estimates may be subject to large uncertainties due to poor estimation of emission factors and the existence of unrecognized sources. As a complement to these inventories, an assessment of emissions at global, national and regional scales can be carried out based on the evaluation of atmospheric measurements and models. This is known as a "top-down" approach. This approach allows linking measured atmospheric concentrations to greenhouse gas fluxes using a transport and chemistry model. It can be used to validate the bottom-up approach. To answer this problematic, and complementary to current and planned exploratory missions, a constellation allowing to increase the spatial and temporal resolution (sub daily global coverage with a small footprint (1 km), imaging capabilities, and high CO_2 (1 ppm) and CH_4 (10 ppb) concentration) is required.

The H2020 SCARBO project (Space CARBon Observatory) aims at solving a key challenge of anthropogenic greenhouse gases (GHGs) monitoring from space: improving the temporal revisit over the various sites of interest while meeting the accuracy and spatial resolution requirements (as per the EU guidelines on anthropogenic GHGs monitoring). To do that, a novel miniaturized static spectrometer concept called NanoCarb is currently being developed to be included on a constellation of small satellites and coupled with aerosol sensors and high-end reference instruments.

In this paper, we present the two prototypes designed to detect and quantify the atmospheric carbon dioxide (CO_2) and methane (CH_4). These are based on a new interferometric architecture, called ImSpoc, patented by ONERA and IPAG [2]. This paper describes the main features of the instruments, and the laboratory calibrations which are carried out to

*florence.de_la_barriere@onera.fr; onera.fr

validate the good quality of the optical components and of the assembly. First results from an airborne campaign are detailed in another paper [3].

Section 2 deals with the design of the prototypes and, in particular, the interferometric architecture. Section 3 depicts measurements made on individual key components. Section 4 describes the tests and calibrations carried out in our laboratory to assess the good quality of the whole assembled NanoCarb prototypes. Section 5 concludes.

2. DESIGN OF THE INSTRUMENT

Both prototypes (for CO_2 and CH_4) are based on the ImSpoc architecture [4-6]. The ImSpoc concept is composed of a phase plate with several steps, arranged as a chessboard, a microlens array (each microlens being associated to one step of the phase plate with a given thickness) and a single focal plane array (FPA) which records the interferometric signal and a set of images of the scene. In order to light the interferometric core with a plane wavefront, a classical way is to use an afocal system, based on at least two lenses. The instruments work in the short-wave infrared (SWIR) around 1.6 µm, which corresponds to absorption bands of CO_2 and CH_4. A diagram of the instrumental concept is shown in Figure 1.

Each microlens is associated to a step of the phase plate, acting as an interferometer with two main waves. The NanoCarb instrument thus produces 10x8 images of the scene on a single FPA, each image corresponding to an area of 60x60 pixels. The specificity of NanoCarb is to measure only few optical path differences (OPD), as many as the number of steps of the interferometric plate; in other words we only measure a partial interferogram. This specificity leads to a paradigm shift, since it is impossible to retrieve the spectrum from a partial interferogram. Therefore, the estimation of the CO_2 (and CH_4) column concentration has to be done directly from these partial interferograms.

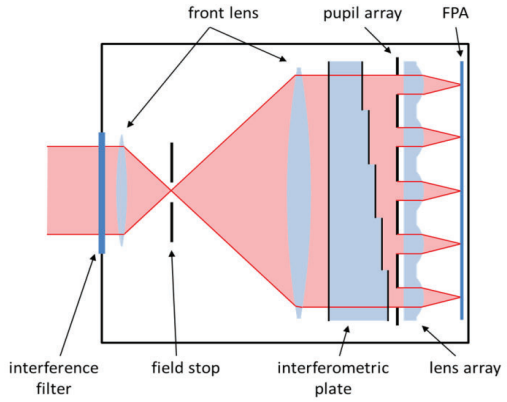

Figure 1. Schematic representation of a spectro-imaging instrument based on the ImSpoc concept.

The following sub-sections describe the optical components and deal with their manufacturability.

2.1 Stepped interferometric phase plate

A key component of the instrument is the stepped interferometric phase plate, whose diagram is shown in Figure 2. We manufacture this component in a monolithic Silicon substrate. The height between two adjacent steps is constant and equal to a few nanometers. The piece is made of 10 x 8 steps, each step has a size corresponding to 60x60 pixels of the FPA. Even though we do not acquire the whole interferogram, we can nevertheless define an equivalent spectral resolution $d\sigma_{eq}$, based on the maximal optical path difference δ_{max}:

$$d\sigma_{eq} = \frac{1}{2\delta_{max}}, \quad (1)$$

δ_{max} can be calculated with the following equation on axis:

$$\delta_{max} = 2 \times n \times e_{max}, \quad (2)$$

where e_{max} is the maximum value of the cavity thickness and n is the group refractive index of the cavity material (Silicon in our case).

For NanoCarb, the equivalent spectral resolution is equal to $d\sigma_{eq}$=0.9 cm^{-1} for the CO_2 prototype and $d\sigma_{eq}$=2.4 cm^{-1} for the CH_4 prototype.

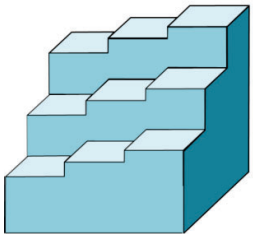

Figure 2. Schematic representation of ImSpoc stepped interferometric phase plate.

2.2 Microlens array

Each step of the interferometric phase plate is associated with a microlens, which focuses light on the FPA and gives the imaging function of the instrument. It produces a set of identical images on the FPA. Thus, the microlens array has the same pitch as the steps of the interferometric phase plate. It is manufactured in a monolithic piece of optical glass. The field of view associated to each microlens is 12°x12°. An afocal front optics adapts the field of view of the whole instrument to 18°x18°.

Table 1 sums up the theoretical optical features of the interferometric core (phase plate and microlens array) of the instrument.

Table 1. Theoretical optical features of the instrument.

Property	Value
Field of view of each microlens	12° x 12°
Number of channels	10 x 8
Number of pixels per channel	60 x 60
Pixel size	15 µm
F-number for each microlens	6.6
Optical quality	Limited by diffraction
Equivalent spectral resolution	0.9 cm^{-1} (CO_2) / 2.4 cm^{-1} (CH_4)
Wavelength range	Around 1.6 µm
Field of view at the afocal entrance	18° x 18°
Magnification of the afocal optics	0.67

2.3 Assembly

The phase plate and the microlens array form what we call the interferometric core. The two components are aligned so that each microlens is in front of one step of the phase plate, and the interferometric core is then assembled near the FPA of the system. The manufactured components and their assembly are shown in Figure 3. The interferometric core is thermally regulated by a unique Peltier module. The spectral filter, which is closely associated to the interferometric core, benefits from this regulation.

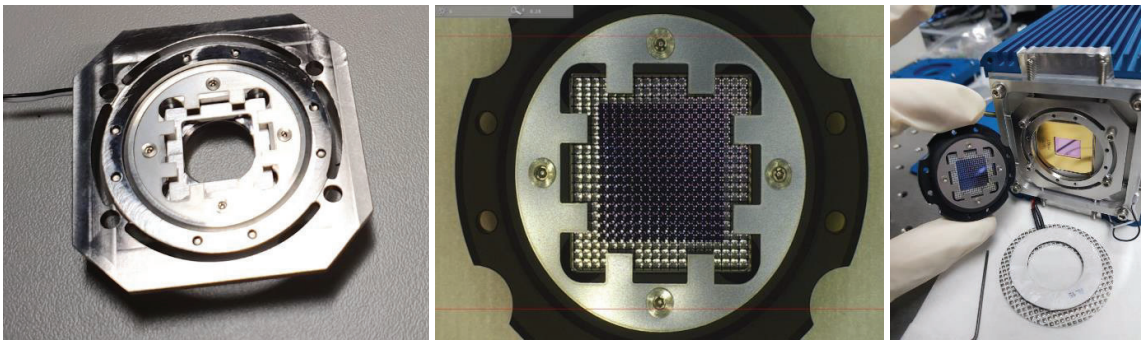

Figure 3. (Left) Mechanical mount of the interferometric core, (Middle) Mounted interferometric core, on the top we can see the microlens array, (Right) The interferometric core and the FPA.

Figure 4 gives a picture of the assembled instrument.

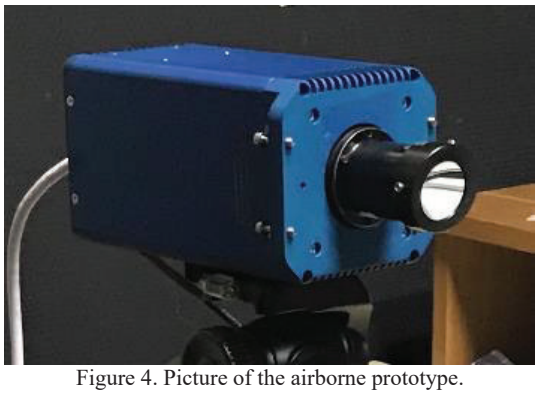

Figure 4. Picture of the airborne prototype.

3. MEASUREMENTS ON KEY INDIVIDUAL COMPONENTS OF NANOCARB

3.1 Spectral filter as a function of the incidence angle

For the airborne prototype, the spectral filtering is shared by two components: a narrow band filter and a broadband filter, this latter being the same for the CO_2 and CH_4 prototypes. To limit stray images, this broadband filter is tilted, so that the reflected light is blocked by the field stop. But this also implies that the range of incidence angles on this filter is wider than the NanoCarb field of view. We have therefore measured the spectral transmission of this filter for angles of incidence (AOI) varying between 0° (normal incidence) and 25°. The results are plotted in Figure 5, left.

The central wavelength varies from 6000 cm^{-1} (1.667 µm) for AOI=0° to 6200 cm^{-1} (1.613 µm) for AOI=25°. The effective index of the filter, used to describe the spectral shift with respect to the angle of incidence, is equal to 1.60. These measurements confirm the theoretical behavior of this broadband filter under different AOI, and the good rejection ratio of this broadband filter, as it appears more clearly on the log plot (Figure 5, right).

About the narrow band filters, they are not tilted, so the range of angles of incidence is lower. However, these filters are much narrower, and the spectral shift relatively to the full-width at half maximum is more significant, as it can be seen in Figure 6. The experimentally estimated effective index is 1.84 for the CH_4 filter and 1.77 for the CO_2 filter.

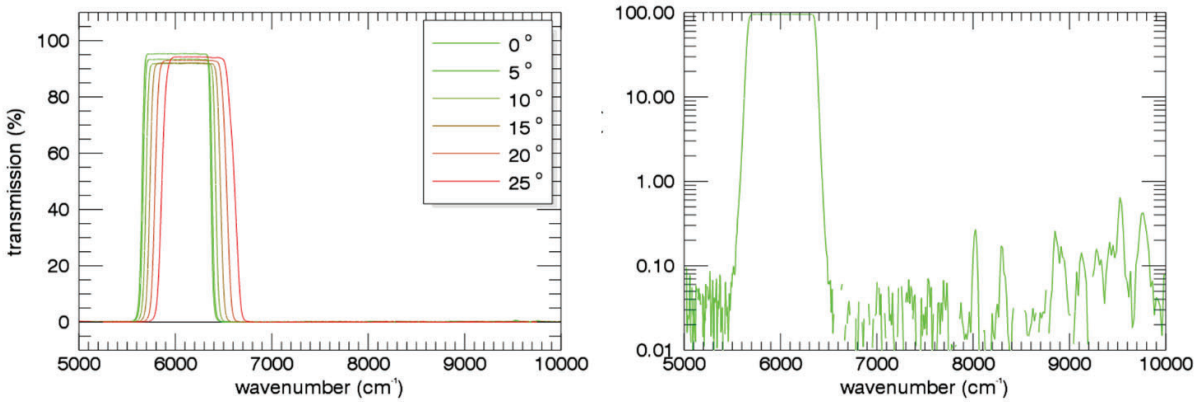

Figure 5. Spectral transmission of the broadband filter of the airborne prototype. Left: dependence with the angle of incidence (AOI) between 0° and 25°. The variation of the maximal transmission with respect to the AOI may be attributed to instabilities of the test bench. Right: on-axis transmission in log scale.

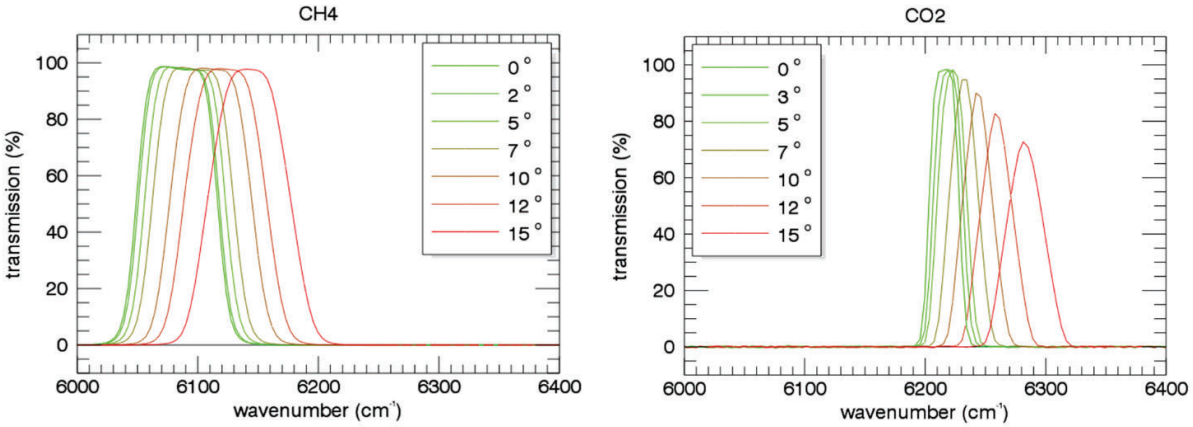

Figure 6. Spectral transmission of the narrow band filters of the airborne CH_4 and CO_2 prototypes.

3.2 Spectral response of the FPA as a function of temperature

We measure the spectral response of the FPA as a function of its temperature, regulated by a Peltier element. The bench is based on a commercial Fourier Transform Infrared (FTIR) spectrometer (model Bruker Vertex 70) and was purposely developed in our laboratory to extract the quantum efficiency of infrared detectors [7]. This experiment allows knowing precisely which temperature has to be set to obtain the desired performance of the instrument during the airborne campaign, especially for the CH_4 prototype, since its spectral band is very close to the cut-off of the InGaAs FPA. Figure 7 gives the normalized spectral response of the FPA of the CH_4 prototype, averaged over the whole pixels, zoomed near the cut-off wavenumber. As expected, this latter decreases as the temperature increases, about -2,2 cm^{-1}/K, slightly less than the expected value of -3.0 cm^{-1}/K [8]. We can check that the CH_4 spectral band is well inside the sensitivity area of the FPA. This measurement is also useful to define the requirement on the temperature stabilization of the FPA.

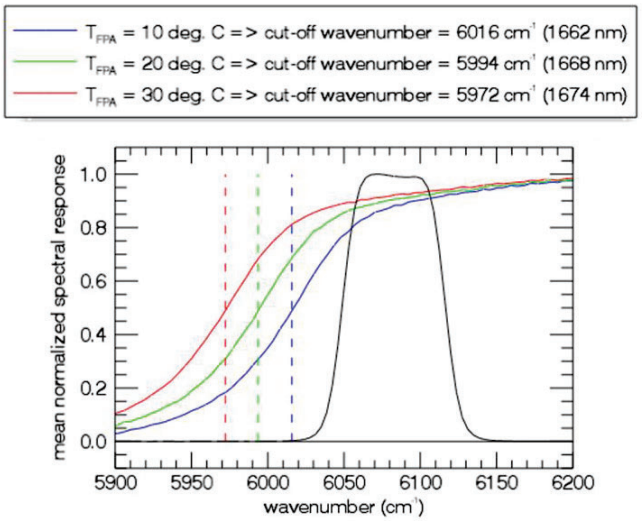

Figure 7. Normalized spectral response of the FPA of the CH_4 prototype, averaged over all the pixels, for three FPA temperatures. The 10°C, 20°C and 30°C are the temperature settings which may differ from the actual FPA temperature. The black curve is the on-axis transmission of the CH_4 narrow band filter.

4. LABORATORY CALIBRATION OF NANOCARB

4.1 Geometric calibration: optical quality and distortion

To assess the optical quality of each channel, we measure the modulation transfer function (MTF) of the two prototypes. The test bench is illustrated in Figure 8. A blackbody illuminates a pinhole placed at the focal point of a collimator to generate a plane wave. The camera is placed at the exit of the collimator on rotation stages to make a two-dimension scanning of the spot. This experimental set-up produces the point spread function (PSF) for each channel of the camera. The modulus of the Fourier transform of the PSF yields the MTF. Measurements can be made for several points in the field of view (FOV) of the camera.

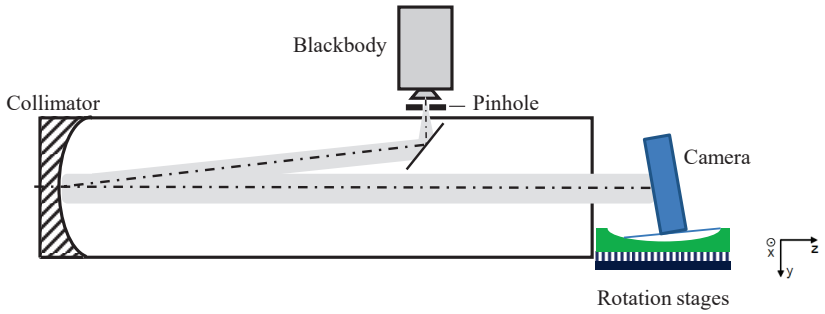

Figure 8. Test bench for PSF/MTF measurements.

Figure 9 shows a raw image delivered by the CO_2 NanoCarb prototype, acquired on the spot scan bench for a point source on axis. On this image, we can see 80 images of the point source. Each image of the point source spreads on a few pixels of the FPA (typically 3x3 pixels). The image acquired by the CH_4 NanoCarb prototype is quite identical.

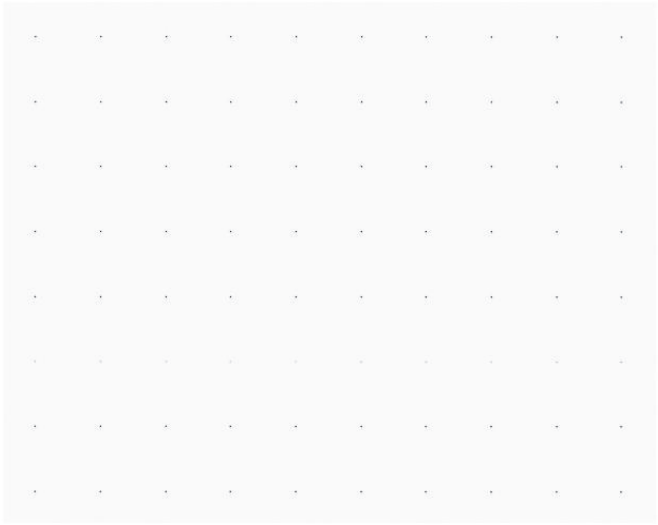

Figure 9. Raw image of a point source acquired on the spot scan bench (inverse contrast). Light is focused at the centre of each subimage. On this image, we see the focal points of the 80 microlenses of the CO_2 NanoCarb prototype.

Figure 10 shows the PSF cross-sections along the horizontal (H) and vertical (V) axes for the 80 channels of the CO_2 NanoCarb prototype. The inset is an example of 2D measured PSF, for one channel. We also show the H and V MTF cross-sections for the 80 channels. The measured MTF is compared to the theoretical one calculated with the Zemax software. The theoretical MTF is close to the expected one, therefore it assets the quality of the assembly. By overlaying the results of the 80 channels, we can see that there is no significant optical disparity between the channels. The same measurements can be made on axis, and within the field of view of the prototype: in this way, we can observe that the optical quality does not degrade within the FOV. The results are shown in Figure 11 and 12. All the channels have very few aberrations. The quality of the system is almost limited by the diffraction.

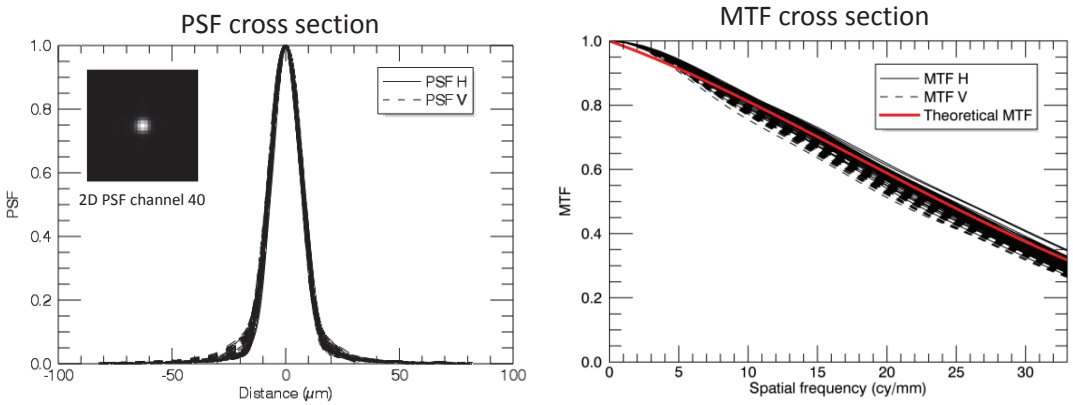

Figure 10. Cross-sections of PSF and MTF for the 80 channels of the CO_2 NanoCarb prototype, compared with the theoretical MTF. Inset: image of measured two-dimensional PSF.

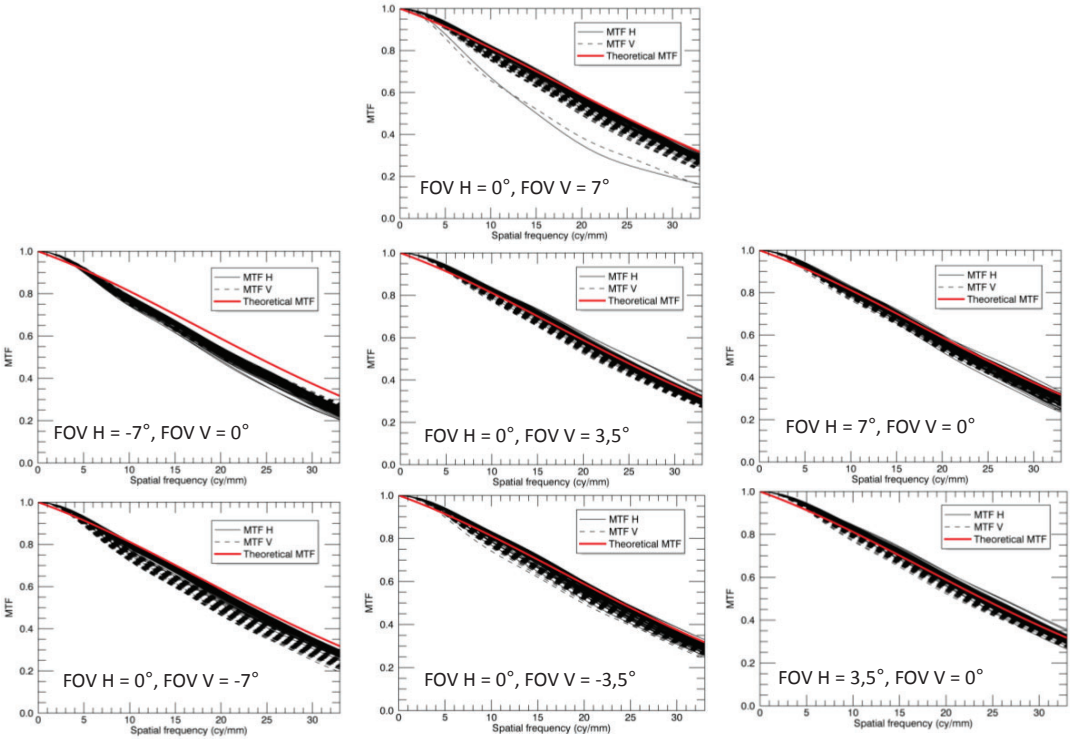

Figure 11. NanoCarb CO_2 prototype: cross-sections of MTF measured within the FOV.

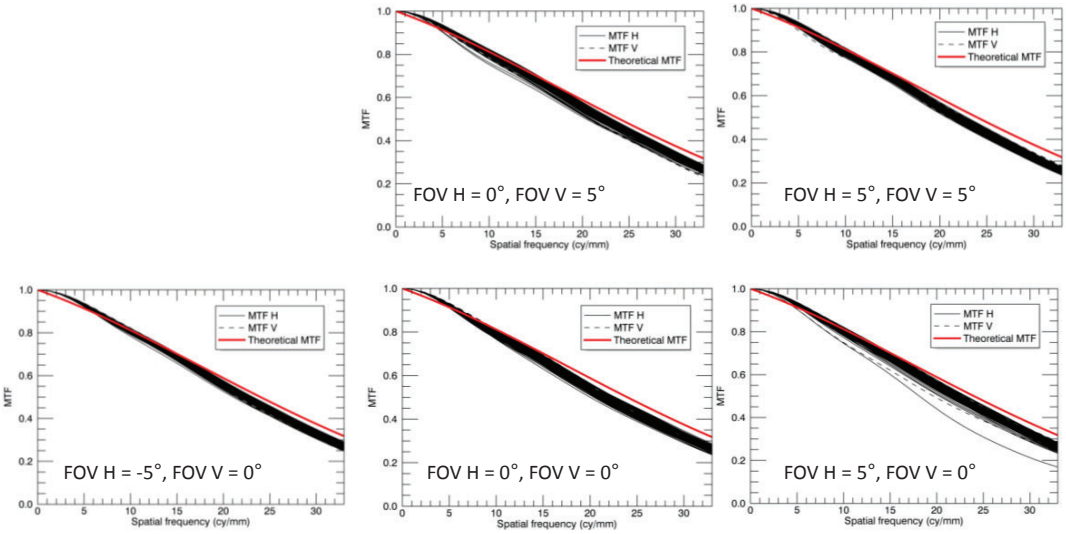

Figure 12. NanoCarb CH_4 prototype: cross-sections of MTF measured within the FOV.

With the rotation stages, we can estimate the horizontal and vertical FOV by moving the point source from an extremity of the detector to the other. We can also estimate the angular resolution IFOV by moving the point source from one pixel to the adjacent pixel. The precision of the rotation stages is equal to 0.001°. However, we can only obtain an estimation

of the FOV and IFOV, because they depend on the observation of the point source, when it appears in the FOV, and thus it depends on the operator. Table 2 sums up the results for the two prototypes.

Table 2. Optical feature estimations of the two airborne prototypes (CO_2 and CH_4).

Feature	CO_2 prototype	CH_4 prototype	Theoretical values	Comments
FOV	FOV H = 19.4° FOV V = 19.5°	FOV H = 19.6° FOV V = 19.6°	18°	Compliant
IFOV	0.27°	0.27°	0.28°	Compliant
Afocal magnification	0.68	0.62	0.67	Compliant
Subimages size	70x70 pixels	70x70 pixels	60x60 pixels	Remark above

The size of the diaphragm in the intermediate focal plane of the afocal optics could have been reduced to limit the overlap between adjacent sub-images.

The spot scan bench also allows the measurement of the distortion and of the line of sight of each pixel of the focal plane array. This latter helps for the registration of all subimages, for the airborne campaign data processing [3].

4.2 Spectral calibration

A key point to process NanoCarb data is to know precisely the spectral response of each pixel. This could be done by thoroughly measuring each component individually (filters, interferometric plate, FPA, as done in Section 3) and combining these measurements thanks to a model of the instrument. However, as a drawback, errors are cumulative, and some effects are ignored (for example those resulting from the association of the components, such as multiple reflections between components). Therefore, we choose to experimentally measure the spectral response of the whole system. This is done thanks to a tunable laser, and an integrating sphere, to have a broad-field measurement (see Figure 13).

Figure 14 illustrates the data acquired by the CH_4 prototype. The spectral response of two pixels is plotted at the top. The interference signal is clearly visible, with a contrast of about 55%, very close to the theoretical one expected with a non-coated Silicon plate. Two monochromatic images are given at the bottom, showing the various subimages. We clearly see that different subimages correspond to different OPD. The ring pattern in each thumbnail is due to the slight dependence of the OPD with the angle of incidence on the interferometric plate (which is not, for NanoCarb, the main way to vary the OPD).

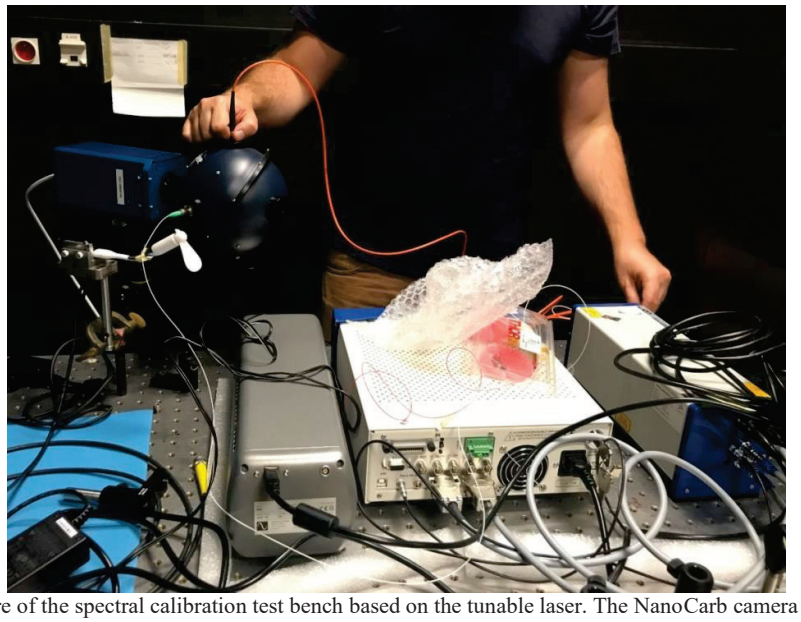

Figure 13. Picture of the spectral calibration test bench based on the tunable laser. The NanoCarb camera is placed on the output port of the integrating sphere, which is lit through an optical fiber by the tunable laser. A wavemeter simultaneously measures the wavelength of the laser.

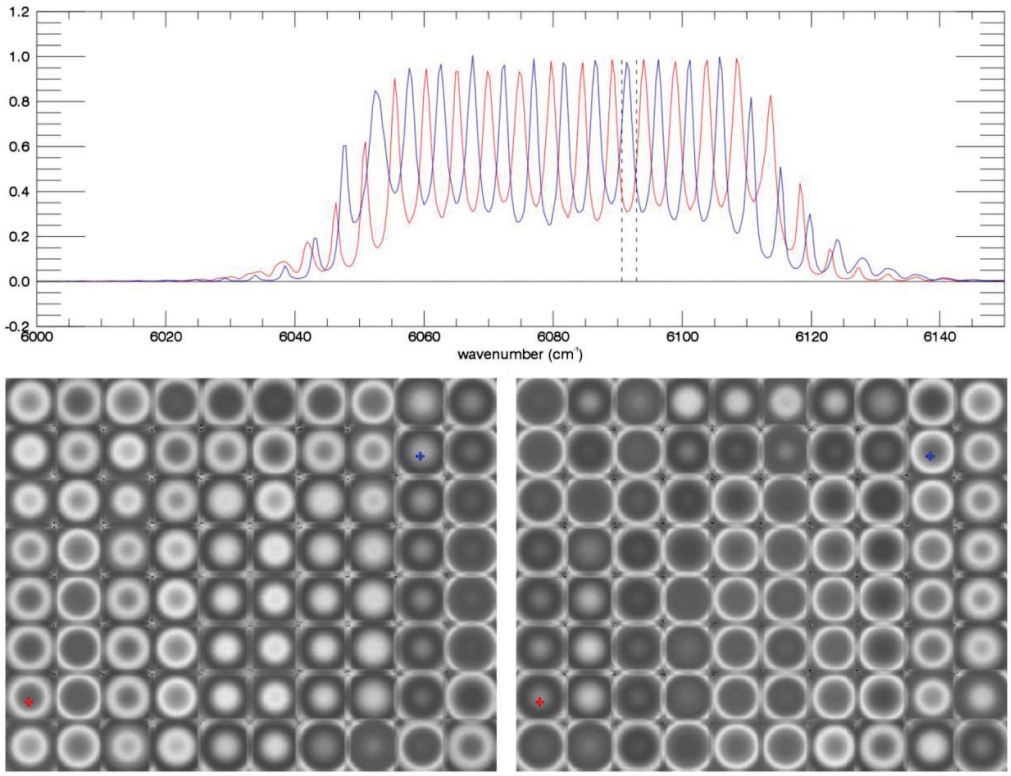

Figure 14. Top: spectral responses of two pixels of the CH_4 prototype. Bottom: monochromatic response of the CH_4 prototype at 6091 cm^{-1} (left) and 6093 cm^{-1} (right), the colored crosses indicate the pixels whose spectral response is plotted above.

4.3 Radiometric calibration

To perform radiometric calibration, the NanoCarb prototype is placed at the exit of an integrating sphere, considered as a homogeneous lambertian surface. The integrating sphere is itself illuminated by a smaller integrating sphere containing the primary source, an halogen lamp emitting light in the visible and SWIR spectral bands. A variable diaphragm allows controlling the radiance at the exit of the main integrating sphere. The radiance has been previously calibrated by the LNE (laboratoire national de métrologie et d'essais, France). A picture of the test bench is given in Figure 15.

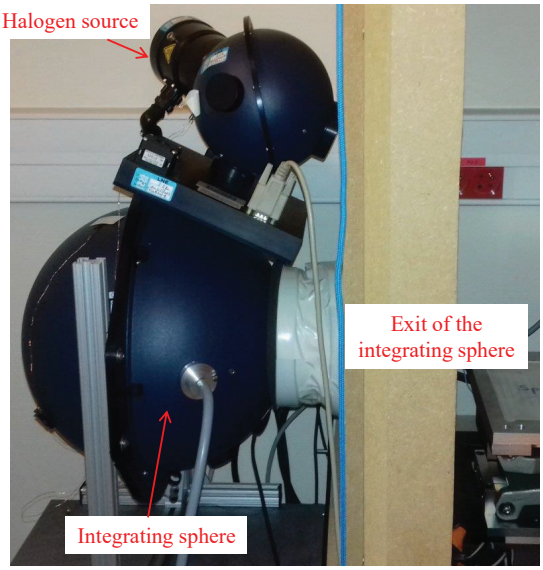

Figure 15. Picture of the calibrated integrating sphere.

These measurements aim at quantifying and correcting the pixels non-uniformities, and calibrating the raw images in radiance. We thus acquire images at various radiances and for various integration times, in order to separate the voltage offset of the electronics from the dark current [9]. Moreover, we systematically acquire sequences of 100 images, in order to have both a higher signal to noise ratio on the mean image, and to estimate the variance of temporal noise.

We used the following simple noise-free instrumental model by pixel:

$$s = d_{offset} + t_i \times [d_{current} + g \int \gamma(\sigma) L(\sigma) \mathrm{d}\sigma] \quad (3)$$

with :

- s [ADU] the raw signal of the pixel;
- d_{offset} [ADU] the offset voltage of the pixel, i.e. the background when the integration time is zero;
- t_i [s] the integration time;
- $d_{current}$ [ADU/s] the dark current of the pixel;
- σ [m^{-1}] the wavenumber;
- $L(\sigma)$ [photons/s/m^2/sr/m^{-1}] the spectral radiance of the scene (assumed to be homogeneous and lambertian);
- $\gamma(\sigma)$ [a.u.] the spectral response of the pixel, as measured in Section **Erreur ! Source du renvoi introuvable.**;
- g [ADU/photons/m^2/sr] the gain of the pixel.

Examples of offset voltage and dark current images are shown in Figure 16.

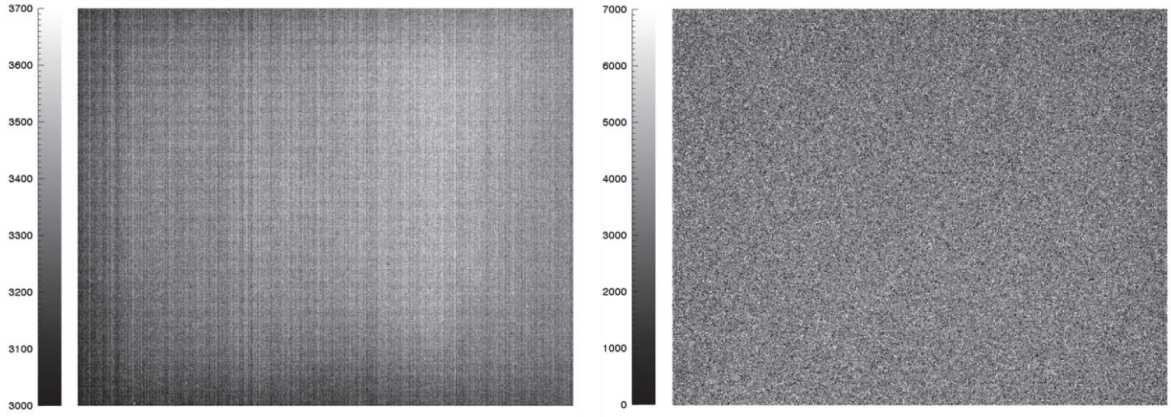

Figure 16. Left: image of the offset voltage [ADU]. The histogram of this image has its maximum at 3390 ADU. Right: image of the background current [ADU/s]. The histogram of this image has its maximum at 3330 ADU/s.

Showing an image of gain g is not relevant, since g is intrinsically related to the measured spectral response $\gamma(\sigma)$: it thus depends on the normalization of $\gamma(\sigma)$ which can arbitrarily vary from one pixel to the next.

The knowledge of the parameters of Equation (3) is sufficient to radiometrically calibrate the signal delivered by a pixel. However, it is interesting to go further to check the consistency of our model, that is to estimate the absolute spectral response $\eta(\sigma)$ of the pixel. $\eta(\sigma)$ is the efficiency of the whole system, in detected electron by incoming photon [electron/photon]. In addition to $\gamma(\sigma)$ and g, we need an estimation of the geometric étendue G [m².sr] and of the quantization step κ of the read-out circuit. κ [electron/ADU] is the number of detected electrons in 1 ADU. We assume that both G and κ are pixel-independent. The geometric étendue is given by the area of the pixel (square of 15 µm) and the F-number of the microlens. About κ, we estimate it by assuming that the noise has two independent origins: a read-out noise and a Poisson noise associated to the numbers of detected electrons. Thus, by plotting the variance of the signal versus the mean of the signal, we can derive κ so that the slope is equal to 1. We find $\kappa = 2{,}50$ electron/ADU. Thus knowing G and κ we can estimate $\eta(\sigma)$ since we have the following identity for the raw flux from the scene [ADU/s]:

$$g \cdot \gamma(\sigma) = \frac{G}{\kappa} \cdot \eta(\sigma) \tag{4}$$

Figure 17 (left) shows the curve used to estimate the quantization step κ and Figure 17 (right) illustrates the absolute spectral response $\eta(\sigma)$ for two pixels from the CO_2 prototype: this spectral response is very consistent with the expected one taking into account the transmission of the optical components and the FPA efficiency, thus validating our model and our estimation of its parameters.

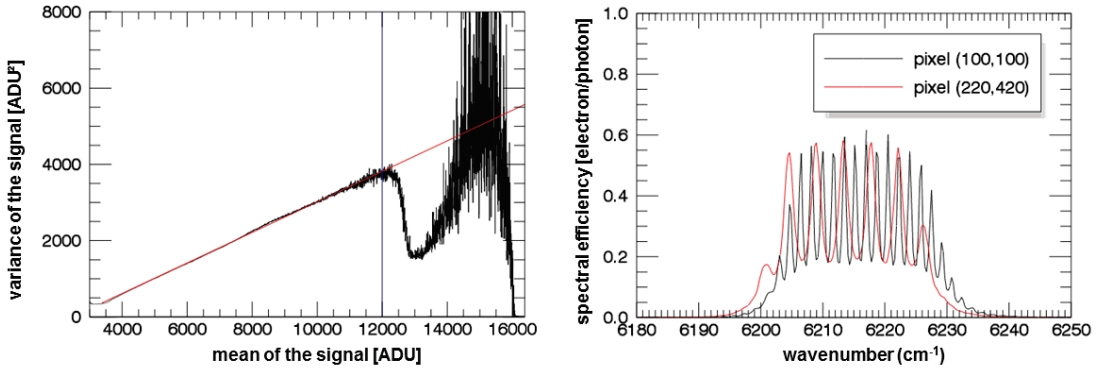

Figure 17. Left: variance of the measured signal [ADU²] versus the mean of the signal [ADU]. This curve is obtained by merging all the pixels. The quantization step κ is derived from the slope of the linear fit. The blue segment indicates the upper bound of the linearity interval. Right: example of the absolute spectral response of one pixel.

5. SUMMARY

In this paper, we have presented a new instrumental concept for a static Fourier Transform spectro-imaging sensor, which is well suited for atmospheric sounding. The interferogram sampling is achieved by a phase plate with several steps, arranged as a chessboard. The imaging capacity is made with a microlens array, each microlens associated to a step of the phase plate, and thus to a given value of optical path difference. This theoretical concept has been applied to build two prototypes for CO_2 and CH_4 monitoring, working around 1.6µm.

These prototypes have been characterized in our laboratory and show good imaging, spectral and radiometric features. They have been used for an airborne campaign. First experimental results are presented in another paper [3].

ACKNOWLEDGEMENTS

NanoCarb initiated in the framework of the LabEx FOCUS ANR-11-LABX-0013.

The SCARBO project has received funding from the European Union's H2020 research and innovation program under grant agreement No 769032, http://scarbo-h2020.eu.

REFERENCES

[1] Ciais, P., *et al.*, "Towards a European operational observing system to monitor fossil CO_2 emissions : final report from the expert group," COPERNICUS, EU publications (October 2015).
[2] Guérineau, N., Le Coarer, E., Ferrec, Y., de la Barrière, F., "Spectro-imageur multivoies à transformée de Fourier," Patent WO2018/002558Al (2018).
[3] Gousset S., Ferrec Y., Rodrigo-Rodrigo J., Croizé L., Le Coarer E., Ehrhardt H., et al., "NanoCarb spaceborne miniaturized GHG sensor: first experimental results," International Conference on Space Optics-ICSO 2020, Proc. SPIE (2021).
[4] Ferrec, Y., Bonnery, G., Brooker, L., Croizé, L., Gousset, S., Le Coarer, E., "NanoCarb part 1: compact snapshot imaging interferometer for CO_2 monitoring from space," International Conference on Space Optics-ICSO 2018, Proc. SPIE 11180, p. 1118021 (2019).
[5] Gousset, S., Le Coarer, E., Guérineau, N., Croizé, L., Laveille, T., Ferrec, Y., "NANOCARB-21: a miniature Fourier-transform spectro-imaging concept for a daily monitoring of greenhouse gas concentration on the Earth surface," International Conference on Space Optics-ICSO 2016 , Proc. SPIE 10562, p. 105624U (2017).
[6] Gousset, S., Croizé, L., Le Coarer, E., Ferrec, Y., Brooker, L., "NanoCarb part 2: Performance assessment for total column CO_2 monitoring from a nano-satellite," International Conference on Space Optics-ICSO 2018, Proc. SPIE 11180, p. 111803Q (2019).
[7] Rommeluère, S., Haïdar, R., Guérineau, N., Deschamps, J., de Borniol, E., Million, A., Chamonal, J. P., and Destefanis, G., "Single-scan extraction of two-dimensional parameters of infrared focal plane arrays utilizing a Fourier-transform spectrometer," Appl. Opt. **46**(9), 1379–1384 (2007).
[8] Paul, S., Roy, J. B., Basu, P. K., "Empirical expressions for the alloy composition and temperature dependence of the band gap and intrinsic carrier density in $Ga_xIn_{1-x}As$," Journal of Applied Physics 69, 827 (1991).
[9] Kattnig, A., Thétas, S., and Primot, J., "Ensuring long-term stability of infrared camera absolute calibration," Optics Express 23, 18381 (2005).